A three-dimensional phenomenological model for shape memory alloys including two-way shape memory effect and plasticity

Giulia Scalet*[a], Fabrizio Niccoli[c], Cedric Garion[c], Paolo Chiggiato[c], Carmine Maletta[b], Ferdinando Auricchio[a]

[a] *DICAr, University of Pavia, 27100 Pavia, Italy, giulia.scalet@unipv.it (corresponding author), auricchio@unipv.it*
[b] *DIMEG, University of Calabria, 87036 Rende (CS), Italy, carmine.maletta@unical.it*
[c] *CERN-European Organization for Nuclear Research, 1211 Geneva 23, Switzerland, fabrizio.niccoli@cern.ch, cedric.garion@cern.ch, paolo.chiggiato@cern.ch*

Abstract

The one-way and two-way shape memory effects (SMEs) as well as the thermal hysteresis represent fundamental properties when dealing with the design of detachable and thermally-stable connection systems based on shape memory alloys (SMAs). Such properties can be induced and tuned by thermo-mechanical processes that include thermal treatments and severe pre-deformation in martensitic state, causing the onset of plastic strains. In such complex conditions, material modeling is of great importance to support the design. This paper proposes a generalization of the three-dimensional phenomenological constitutive model by Souza et al. (1998), in order to describe the behavior of severely pre-strained NiTi-based SMAs. The proposed model allows to describe pseudoelasticity, one-way and two-way SMEs, as well as additional physical phenomena evidenced experimentally, such as transformation temperatures' evolution, thermal hysteresis, phase transformations at low stresses, thermal strains, and phase-dependent elastic properties. Several numerical simulations, ranging from uniaxial tests to the finite element analysis of two case-studies, are performed. Model results are in good agreement with the results of a performed experimental campaign and allow to discuss SMA behavior under such complex loading conditions.

Keywords: shape memory alloys, one-way shape memory effect, two-way shape memory effect, plasticity

1. Introduction

Shape Memory Alloys (SMAs) are widely applied in various fields of engineering and medicine thanks to their unique strain recovery capabilities (Duerig et al., 1990; Jani et al., 2014; Otuska and Wayman, 1998), that can be obtained either by heating or by stress release, through the so-called Shape Memory Effect (SME) and Pseudoleastic Effect (PE), respectively. SME and PE are due to reversible solid-state microstructural transitions, the so-called thermoelastic martensitic transformations (TMT), betwen the parent body-centered cubic austenitic phase (B2) and the product monoclinic martensitic one (B19'). TMT can be induced either by temperature changes (TIM, Thermally-Induced Martensite) or by mechanical loads (SIM, Stress-Induced Martensite), providing the SME and PE, respectively. B2 phase is stable at high temperature and low stress, while B19' is stable at low temperature and high stress. Thanks to TIM, the material is able to change its microstructure reversibly when varying the temperature between the so-called Transformation Temperatures (TTs). Direct transformation (B2-B19') can occur when cooling the material below the martensite TTs, while reverse transformation takes place during heating above the austenite TTs. The difference between martensite and austenite TTs, namely ΔTT, is regarded as the thermal hysteresis of the material.

Thermal hysteresis, and the associated stress-strain hysteresis, is a limiting phenomenon in SMA-based fast actuation systems, as it represents a source of inefficiencies due to the increased energy loss and time response. Nevertheless, thermal hysteresis could be a beneficial feature when a large thermal stability range is needed, such as in some fasteners or connectors operating in constrained recovery mode (Duerig et al., 1990; Humbeeck, 2001; Jani et al., 2014).

In such systems recovery forces are generated as the SMA element, previously deformed in martensitic state, is heated up to the austenite TTs in a constrained shape, i.e. against a mechanical obstacle. This is due to the so-called One-Way Shape Memory Effect (OW-SME) and it is the basic principle of many successful systems, e.g. permanent fasteners, couplers, or SMA hybrid composites (Duerig et al., 1990; Humbeeck, 2001; Jani et al., 2014; Kirkby et al., 2008).

Differently, the so-called Two-Way Shape Memory Effect (TW-SME) offers the unique possibility to obtain detachable devices, operating without biasing elements. In fact, such an effect describes the ability of the SMA

element to change its shape reversibly during subsequent thermal cycles between its TTs, under zero mechanical load.

As a consequence, the OW-SME, TW-SME and ΔTT are very important design parameters when dealing with detachable and thermally-stable SMA-based connection systems. In fact, the wider is the thermal hysteresis (ΔTT), the larger is the temperature range in which the SMA element can exert high recovery forces without undergoing reverse thermal-induced transformations with consequent stress/strain relaxations. Additionally, cooling down to martensite TTs allows the coupler to be dismounted thanks to the TW-SME.

Such properties can be induced and properly tuned by thermo-mechanical processes, the so-called training, which include thermal treatments and severe pre-deformation in martensitic state. The residual stresses associated with the internal plastic strains occurring during training are directional, thus having the potential to accommodate the nucleation of preferentially oriented martensitic variants (Liu et al., 1998; Liu and McCormick, 1990; Otsuka and Ren, 2005; Otuska and Wayman, 1998; Tan and Liu, 2004), leading to the development of the TW-SME at the macroscopic scale. Various commercial and non-commercial detachable fasteners and connectors exhibit intrinsic TW-SME (Duerig et al., 1990; Malukhin et al., 2012; Niccoli et al., 2017a,b; Tabesh et al., 2018). In addition, a severe martensitic pre-strain stabilizes the martensitic variants (Lin and Wu, 1993; Liu and McCormick, 1990; Piao et al., 1993; Tan and Liu, 2004), leading to an increase of the austenite TTs and, consequently, of the thermal hysteresis ΔTT. However, this phenomenon is observed only at the first activation cycle (heating stage), while TTs are restored to their initial value (undeformed state) at the subsequent thermal cycles.

Therefore, NiTi alloys represent viable candidates for the realization of SMA-based fasteners or connectors, since they inherently possess good mechanical and shape recovery properties and their intrinsic narrow hysteresis (50°C max) can be properly enlarged by martensitic pre-strain (Lin and Wu, 1993; Piao et al., 1993; Siegert et al., 2003; Tan and Liu, 2004; Wang et al., 2012). However, great attention should be devoted to the material selection and training process. In fact, recovery stress in polycrystalline SMAs is not a material constant and depends significantly on both microstructure and thermo-mechanical history of the alloy, i.e. on the martensitic pre-strain and prevented strain values, the operating thermal cycles (Otuska and Wayman, 1998; Šittner et al., 2000; Yan et al., 2016; Yan and Van Humbeeck,

2013), as well as the mechanical properties of the obstacle (stiffness and thermal expansion). It is generally accepted and experimentally verified (Duerig et al., 1990; Šittner et al., 2001, 2000) that, during the constrained recovery mechanism, most of the detwinned martensite variants, induced during the pre-strain phase, transform to austenite by heating. Recovery stress increases almost linearly with temperature (Duerig et al., 1990; Šittner et al., 2001, 2000), reaching its maximum values at a temperature at which the reoriented martensite is not anymore thermally-stable. Consequently, if maximum recovery forces are needed, a significant accumulation of plastic strains could occur during constrained heating. Such plastic strains play a very important role on both mechanical and functional response of SMA devices.

In conclusion, severely pre-strained NiTi alloys could be possible candidates for the development of detachable fasteners or connectors when the following criteria are satisfied: (a) suitable OW-SME to allow the generation of sufficiently high recovery forces; (b) austenite TTs sufficiently higher than the service temperature (T_0) to avoid possible accidental activation (Xu et al., 2003) during material handling/manipulation; (c) martensite TTs sufficiently lower than T_0 to avoid stress/strain relaxations during service (wide thermal stability range); (d) suitable TW-SME to allow thermal dismounting during cooling below martensite TTs, even without a resetting bias element. Certainly, the functional response of these NiTi-based devices, in terms of TTs, OW-SME, and TW-SME, need to be tailored specifically for each application as the reliability and stability of the SMA element is directly related to the magnitude and evolution of the recovery strain/stress.

Within this framework, the focus of the present paper is the modeling of the behavior of severely pre-strained NiTi alloys to support the design of new detachable fasteners or connectors. As discussed above, the response of these alloys in terms of TTs, OW-SME, and TW-SME (even without a resetting bias element) is mainly affected by the plastic strain occurring during severe martensitic pre-strain and possible subsequent constrained thermal cycles (high recovery stress generation).

In order to account for irrecoverable strains, SMA modeling approaches generally concern the description of (i) transformation-induced plasticity due to cyclic thermo-mechanical transformation or (ii) plastic strains associated with slip mechanisms at sufficiently high stresses (i.e. yield stresses). To describe (i), current works propose simple relationships (Hebda and White, 1995; Rogueda et al., 1991), one-dimensional models (Auricchio et al., 2003), and three-dimensional models (Ashrafi, 2019; Auricchio et al., 2007; Bar-

rera et al., 2014; Bo and Lagoudas, 1999; Heller et al., 2019; Lagoudas and Entchev, 2004; Lexcellent et al., 2000; Saint-Sulpice et al., 2007; Sehitoglu et al., 2000; Xu et al., 2019; Zaki and Moumni, 2007), where the evolution of transformation-induced plastic variables generally depends on phase transformation and the number of cycles. To describe (ii), one-dimensional (Govindjee and Kasper, 1997; Jiang and Landis, 2016; Paiva et al., 2005) and three-dimensional (Hartl and Lagoudas, 2009; Khalil et al., 2012; Petrini et al., 2017; Wang et al., 2007; Yan et al., 2003; Zhang et al., 2007) models have been proposed. These models generally assume that martensitic transformation and plastic slip occur simultaneously or, alternatively, that plastic strain formation takes place when phase transformation is completed.

Given our focus, the description of transformation-induced plasticity and of SMA response under any type of cyclic loading, i.e. (i), is beyond the scope of this work and it is not accounted for. Contrarily, our attention is dedicated to the description of plastic strains at sufficiently high stresses, i.e. (ii). Particularly, to the authors' knowledge, the analysis of the effect of plastic deformation, occurring during severe martensitic pre-strain and possible subsequent constrained thermal cycles, on the OW-SME, TW-SME, and TTs is not considered in the modeling literature and it is the contribution of the proposed paper.

Motivated by the discussed framework, the present paper aims to develop a three-dimensional phenomenological constitutive model to simulate both SIM and TIM mechanisms coupled with plasticity in severely pre-strained SMAs.

The proposed formulation starts from the three-dimensional small-strain phenomenological model proposed by Souza et al. (1998), which is able to capture main SMA features, i.e., PE, OW-SME, and TW-WAY under an applied load. The choice of extending the model by Souza et al. (1998) is dictated by its simple formulation requiring just one tensorial variable, namely the transformation strain, describing the macroscopic strain due to TIM or SIM transformations between a generic parent phase and a product phase, and by its low number of parameters (just seven). These advantages have promoted numerous contributions, including mathematical considerations, numerical methods, engineering simulations, and model generalizations, see Grandi and Stefanelli (2015) and references therein. Specifically, it is worth highlighting the generalizations by Ashrafi (2019); Auricchio et al. (2007); Barrera et al. (2014) to include transformation-induced plasticity and by Petrini et al. (2017) to include also plastic strains at sufficiently high stresses

for biomedical applications based on PE. However, no extensions of the model by Souza et al. (1998) have been proposed in order to describe the response of severely pre-strained NiTi alloys.

For our purpose, a new tensorial internal variable, i.e. the plastic strain, is added to describe the macroscopic strain due to plastic effects. Constitutive equations and evolution laws are then written in a thermodynamically-consistent framework and a physical interpretation of model parameters is provided. Also, model formulation includes several additional phenomena in material behavior, namely, low-stress phase transformations, phase-dependent material properties, and thermal strains. Accordingly, the proposed model is able to capture the thermo-mechanical behavior of severely pre-strained SMAs in both free and constrained recovery condition. The model describes the behavior of the alloy in the first stress-free/stress applied thermo-mechanical cycle after martensitic pre-deformation.

Several numerical simulations are performed, including uniaxial tests and the finite element analysis of two case-studies, i.e. a ring-shaped coupler and a C-shaped fastener. Results from numerical simulations of uniaxial isothermal tests as well as free and constrained thermal recovery are validated through a comparison with data from a performed experimental campaign on a NiTi-based alloy. Various aspects of SMA behavior, in particular in the case of severe martensitic pre-deformation and thermally-induced recovery strain/stress generation, are analyzed and discussed.

The paper is organized as follows. Section 2 presents the results of the performed experimental campaign. Sections 3 and 4 present model equations, respectively, in a time-continuous and discrete setting. Section 5 discusses the results of numerical simulations. Conclusions are given in Section 6.

2. Materials and experiments

The material used in this investigation is a Ni rich NiTi alloy (50.8Ni-49.2Ti % at.). Figure 1 shows the DSC thermogram and TTs of the alloy after a full annealing process (T = 900°C for 45 min). The alloy has a complete austenitic structure at room temperature ($A_f = 12$°C) and a narrow thermal hysteresis ($A_p - M_p \sim 30$°C).

As discussed in Section 1, the austenite TTs can be increased, at least at the first thermal cycle, by severe pre-strain in martensitic condition. This mechanism has been systematically investigated by proper thermo-mechanical tests. The tests were carried out by a universal testing machine

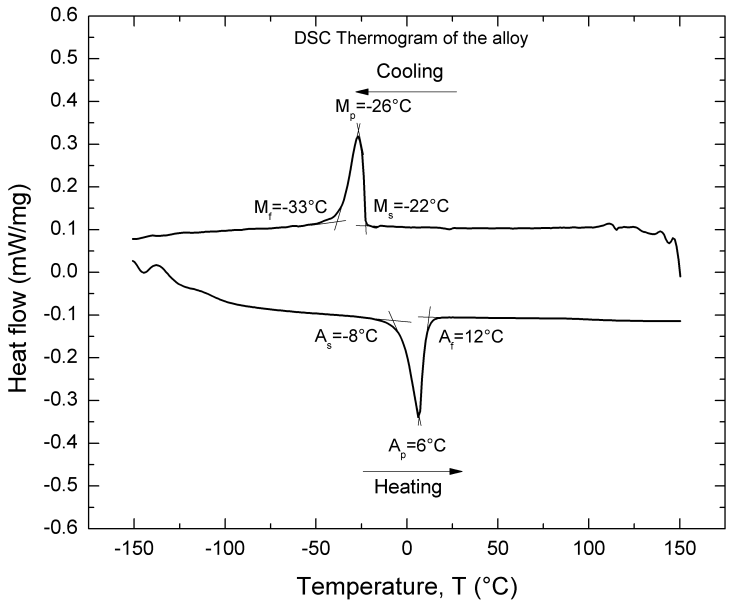


Figure 1: Differential Scanning Calorimetry thermogram of the investigated NiTi alloy.

(Instron E10000, 10 kN), equipped with a thermal chamber (-170°C/ $+$ 350°C). Uniaxial NiTi specimens (dogbone-shaped samples with 10 mm gauge length and 4.5 mm^2 cross section) were used and strain and temperature were measured/controlled by an extensometer and a k-type thermocouple, respectively. Low temperature mechanical pre-strain was carried out in fully martensitic conditions ($T < M_f$), by monotonic strain controlled ($\dot{\varepsilon} = 5 * 10^{-4}\text{s}^{-1}$) tensile loading up to a given strain, ε_{tot}, followed by complete load-controlled unloading ($\dot{\sigma} = 10$ MPa$\cdot$s^{-1}). Stress-free thermal cycles ($\dot{T} = 2 * 10^{-2}$°C$\cdot$s^{-1}) were carried out after mechanical pre-strain to measure both the TTs and the shape recovery capabilities of the alloy, in terms of one-way (OW) and two-way (TW) shape memory strain (respectively, ε_{OW} and ε_{TW}).

Figure 2 reports a complete thermo-mechanical cycle for $\varepsilon_{tot} = 28.8\%$. The first heating from $T < M_f$ to about 100°C causes the reverse martensite-austenite (M-A) transformation, giving the OW recovery strain ε_{OW} and the permanent strain ε_P, formed during isothermal mechanical pre-strain. It is worth noting that the measured strain recovery includes the thermal strains ($\varepsilon_{TH} = \alpha\Delta T$) which are, however, two order of magnitude lower than ε_{tot}. The austenite TTs of the pre-strained material at the first cycle, namely A_s^{1st}

and A_f^{1st}, are also measured. Subsequent cooling down to -70 $°C$ causes the direct austenite-martensite (A-M) transformation and allows to measure the TW shape memory strain ε_{TW}. The martensite TTs (M_s and M_f) are also measured from the strain-temperature curves. Finally, the second re-heating gives the austenite TTs of the alloy (A_s and A_f) at the second transformation cycle. It was found that no significant variations in both martensite and austenite TTs are observed upon subsequent thermal cycles, i.e. they can be regarded as the stabilized TTs of the alloy. However, slight difference with respect to the base untrained material, i.e. those obtained from DSC in Figure 1, can be obtained.

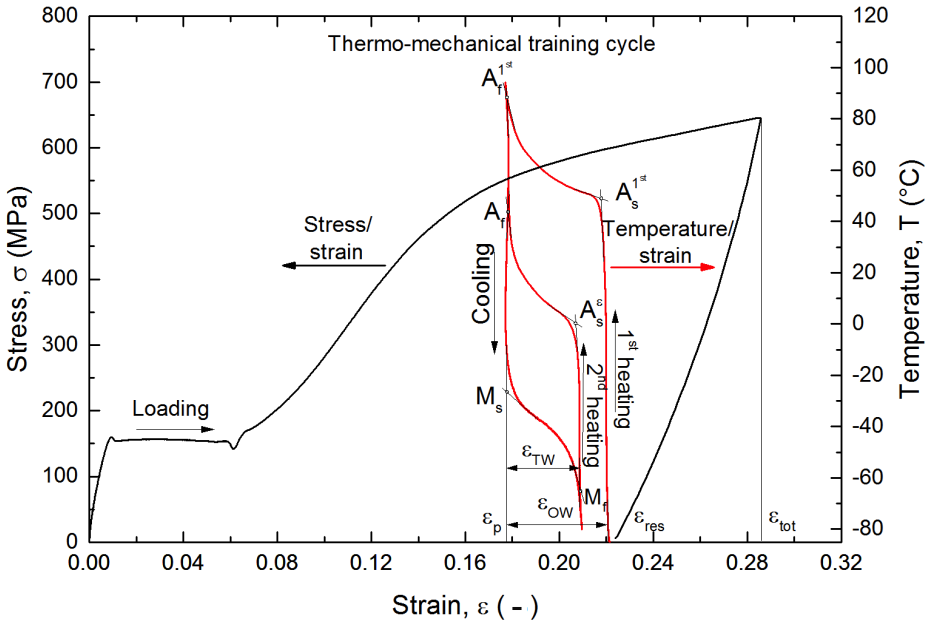


Figure 2: Thermo-mechanical training cycle ($\varepsilon_{tot} = 28.8\%$) on the investigated NiTi alloy.

In the following, for application purposes, our attention will be focused on the modeling of the NiTi alloy response in the first stress-free/stress applied thermomechanical cycle after martensitic pre-deformation.

3. Model formulation

The present section focuses on the time-continuous formulation of the proposed model; see Auricchio and Petrini (2004); Evangelista et al. (2009); Souza et al. (1998) for details about the original model equations.

3.1. Free-energy function

The model assumes the total strain $\boldsymbol{\varepsilon}$ and the absolute temperature T as control variables, while the transformation strain $\boldsymbol{e}^{tr}$ and the plastic strain $\boldsymbol{e}^{p}$ as internal ones. Both $\boldsymbol{e}^{tr}$ and $\boldsymbol{e}^{p}$ are symmetric trace-free second-order tensors.

Specifically, the transformation strain $\boldsymbol{e}^{tr}$ describes the deformation associated to TIM or SIM transformations between a generic parent phase and a generic product phase and allows to take into account in an approximated form the martensite reorientation process (Auricchio and Petrini, 2004). The transformation strain $\boldsymbol{e}^{tr}$ is required to satisfy the following constraint:

$$\|\boldsymbol{e}^{tr}\| < \varepsilon_L \tag{1}$$

ε_L being a positive parameter describing the maximum transformation strain obtainable through alignment of the martensite variants and $\|\cdot\|$ being the Euclidean norm.

The plastic strain $\boldsymbol{e}^{p}$ is the new variable compared to the original model (Souza et al., 1998) and gives a measure of the plastic deformation during specific thermo-mechanical conditions, as severe pre-strain or constrained thermal heating.

The total strain is assumed to be additively decomposed as follows:

$$\boldsymbol{\varepsilon} = \boldsymbol{\varepsilon}^{e} + \boldsymbol{\varepsilon}^{th} + \boldsymbol{e}^{tr} + \boldsymbol{e}^{p} \tag{2}$$

where $\boldsymbol{\varepsilon}^{e}$ and $\boldsymbol{\varepsilon}^{th}$ are the elastic and thermal strain, respectively. The thermal strain is assumed as $\boldsymbol{\varepsilon}^{th} = \alpha \boldsymbol{I}\,(T - T_0)$, where α is the thermal expansion coefficient and T_0 is the initial temperature.

The Helmoltz free energy function $\Psi = \Psi(\boldsymbol{\varepsilon}, T, \boldsymbol{e}^{tr}, \boldsymbol{e}^{p})$ is expressed as the sum of the following terms:

$$\begin{aligned} \Psi = \frac{1}{2}\, K\, \theta^2 + G\, \|\boldsymbol{e} - \boldsymbol{e}^{tr} - \boldsymbol{e}^{p}\|^2 - 3\alpha K \theta\,(T - T_0) \\ + \tau_M\, \|\boldsymbol{e}^{tr}\| + \frac{1}{2}\, h^{tr}\, \|\boldsymbol{e}^{tr}\|^2 + \frac{1}{2}\, h^{p}\, \|\boldsymbol{e}^{p}\|^2 - B\boldsymbol{e}^{tr} : \boldsymbol{e}^{p} + \mathcal{I}_{\varepsilon_L}(\boldsymbol{e}^{tr}) \end{aligned} \tag{3}$$

where θ and $\boldsymbol{e}$ are the volumetric and deviatoric strain, respectively; K and $G = G(\boldsymbol{e}^{tr})$ are the bulk and shear modulus, respectively (details are given in Section (3.4)); $\tau_M = \beta\langle T - T^{*}\rangle$, where $\beta > 0$ is a parameter defining the dependence of the critical stress on temperature, T^{*} is the transformation

temperature, and $\langle\cdot\rangle$ is the positive part function; h^{tr} and h^{p} define, respectively, phase transformation and plastic hardening (they can be interpreted as linear kinematic hardening parameters, as in standard elastoplastic models); $B > 0$ is a parameter that controls the interaction between phase transformation and plastic effects. To keep the model as simple as possible and to limit the number of involved parameters, plastic hardening is here assumed to be linear and the related parameter h^{p} is independent of phase transformation. However, it is recalled that other plastic yield hardening forms can be considered according to experimental evidences (Hartl and Lagoudas, 2009).

The indicator function $\mathcal{I}_{\varepsilon_L}(\boldsymbol{e}^{tr})$ is included in Eq. (3) to satisfy constraint (1):

$$\mathcal{I}_{\varepsilon_L}(\boldsymbol{e}^{tr}) = \begin{cases} 0 & \text{if } \|\boldsymbol{e}^{tr}\| \leq \varepsilon_L \\ +\infty & \text{otherwise} \end{cases} \tag{4}$$

Recall that the Helmoltz free energy in Eq. (3) is strictly convex provided that:

$$h^{tr}h^{p} - B^2 > 0 \tag{5}$$

3.2. Constitutive equations

Following classical theory, the stress-strain relation is obtained by differentiating the free energy function Ψ with respect to the total strain $\boldsymbol{\varepsilon}$, yielding the hydrostatic and deviatoric stresses, respectively as:

$$p = \frac{\partial \Psi}{\partial \theta} = K\theta - 3\alpha K\left(T - T_0\right) \tag{6}$$

$$\boldsymbol{s} = \frac{\partial \Psi}{\partial \boldsymbol{e}} = 2G(\boldsymbol{e} - \boldsymbol{e}^{tr} - \boldsymbol{e}^{p}) \tag{7}$$

Similarly, the thermodynamic forces $(\boldsymbol{X}, \boldsymbol{Y})$ associated to the internal variables $(\boldsymbol{e}^{tr}, \boldsymbol{e}^{p})$ are defined by:

$$\begin{cases} \boldsymbol{X} = -\dfrac{\partial \Psi}{\partial \boldsymbol{e}^{tr}} = \boldsymbol{s} - \dfrac{\partial G}{\partial \boldsymbol{e}^{tr}}\,\|\boldsymbol{e} - \boldsymbol{e}^{tr} - \boldsymbol{e}^{p}\|^2 - \tau_M \dfrac{\boldsymbol{e}^{tr}}{\|\boldsymbol{e}^{tr}\|} - h^{tr}\boldsymbol{e}^{tr} + B\boldsymbol{e}^{p} - \gamma\dfrac{\boldsymbol{e}^{tr}}{\|\boldsymbol{e}^{tr}\|} \\ \boldsymbol{Y} = -\dfrac{\partial \Psi}{\partial \boldsymbol{e}^{p}} = \boldsymbol{s} - h^{p}\boldsymbol{e}^{p} + B\boldsymbol{e}^{tr} \end{cases} \tag{8}$$

where variable γ is defined as follows:

$$\gamma = \begin{cases} 0 & \text{if } \|\boldsymbol{e}^{tr}\| < \varepsilon_L \\ \geq 0 & \text{if } \|\boldsymbol{e}^{tr}\| = \varepsilon_L \end{cases} \tag{9}$$

that yields $\partial \mathcal{I}_{\varepsilon_L}(\boldsymbol{e}^{tr}) = \gamma \boldsymbol{e}^{tr}/\|\boldsymbol{e}^{tr}\|$. Thermodynamic forces $\boldsymbol{X}$ and $\boldsymbol{Y}$ are the work-conjugates to $\boldsymbol{e}^{tr}$ and $\boldsymbol{e}^{p}$, respectively, and are symmetric, deviatoric tensorial quantities. Particularly, $\boldsymbol{X}$ and $\boldsymbol{Y}$ are the driving forces for phase transformation and plastic strain formation processes, respectively. Moreover, it is worth highlighting that the terms $\partial G/\partial \boldsymbol{e}^{tr}\ \|\boldsymbol{e} - \boldsymbol{e}^{tr} - \boldsymbol{e}^{p}\|^2 + \tau_M \boldsymbol{e}^{tr}/\|\boldsymbol{e}^{tr}\| + h^{tr}\boldsymbol{e}^{tr} - B\boldsymbol{e}^{p} + \gamma \boldsymbol{e}^{tr}/\|\boldsymbol{e}^{tr}\|$ in Eq. $(8)_1$ and $h^{p}\boldsymbol{e}^{p} - B\boldsymbol{e}^{tr}$ in Eq. $(8)_2$ can be interpreted as back-stresses, as in standard plasticity, and are the key to the phase transformation-plasticity coupling. From these expressions, it can be observed that parameter B couples the two thermodynamic forces and, thus, the evolution of the two processes. As an example, it contributes to phase transformation under stress-free conditions.

3.3. Limit functions and evolution laws

To describe phase transformation/martensite reorientation, and plasticity evolution, two classical Mises-type limit functions $F_X = F_X(\boldsymbol{X})$ and $F_Y = F_Y(\boldsymbol{Y})$ are introduced in the following form:

$$F_X = \|\boldsymbol{X}\| - R_X \tag{10}$$

$$F_Y = \|\boldsymbol{Y}\| - R_Y \tag{11}$$

where $R_X = R_X(T)$ and $R_Y = R_Y(T)$ are elastic domain radii (details are given in Section (3.4)).

The associative evolution equations for $\boldsymbol{e}^{tr}$ and $\boldsymbol{e}^{p}$ are expressed in the following form:

$$\dot{\boldsymbol{e}}^{tr} = \dot{\xi}\frac{\partial F_X}{\partial \boldsymbol{X}} = \dot{\xi}\frac{\boldsymbol{X}}{\|\boldsymbol{X}\|} \tag{12}$$

$$\dot{\boldsymbol{e}}^{p} = \dot{\mu}\frac{\partial F_Y}{\partial \boldsymbol{Y}} = \dot{\mu}\frac{\boldsymbol{Y}}{\|\boldsymbol{Y}\|} \tag{13}$$

where $\dot{\xi}$ and $\dot{\mu}$ are positive consistency parameters.

Model equations are completed by the Kuhn-Tucker and consistency conditions:

$$\dot{\xi} \geq 0, \quad F_X \leq 0, \quad \dot{\xi}F_X = 0, \quad \dot{\xi}\dot{F}_X = 0 \tag{14}$$

$$\dot{\mu} \geq 0, \quad F_Y \leq 0, \quad \dot{\mu}F_Y = 0, \quad \dot{\mu}\dot{F}_Y = 0 \tag{15}$$

3.4. Model parameters

The proposed model is based on parameters that can be physically interpreted and calibrated from experimental data. It is highlighted that, compared to the original model Souza et al. (1998), three additional material parameters, h^p, B, and R_Y, are introduced for the sake of modulating plastic strains. Details about original model parameters (i.e. K, G, α, β, T^*, R_X, ε_L, h^{tr}) can be found in Auricchio et al. (2009a), while new parameters (i.e. h^p, B, R_Y) can be derived from the experimental evidences described in Section 2, as detailed below.

In particular, the following parameters need to be calibrated:

- Parameter α, describing the thermal expansion coefficient, can be measured experimentally, as done classically.

- Parameters β and T^*, such that $\tau_M = \beta\langle T - T^*\rangle$, can be calibrated from a uniaxial shape memory test under constant stress or knowing the austenite finishing temperature (Auricchio et al., 2009a).

- Parameter $R_X = R_X(T)$, expressing the elastic domain radius governing phase transformation, is assumed to depend on temperature, according to the following definition given by Auricchio et al. (2009a):

$$R_X = \begin{cases} R_{XL} & \text{if } T \leq \left(T^* - \dfrac{\Delta R}{\beta}\right) \\ \beta\,(T - T^*) + R_{XH} & \text{if } \left(T^* - \dfrac{\Delta R}{\beta}\right) \leq T \leq T^* \\ R_{XH} & \text{if } T \geq T^* \end{cases} \tag{16}$$

  where R_{XL} and R_{XH} are the two positive elastic radii at low and high temperatures and $\Delta R = R_{XL} - R_{XH}$ (see Figure 3.a). As reported in Auricchio et al. (2009a), R_{XL} can be calibrated from a uniaxial tensile curve in the fully-martensitic state at $T < T^* - \Delta R/\beta$ (see also Figure 3.a), while R_{XH} from the hysteresis width during a uniaxial shape memory test under constant stress.

- Mechanical properties (i.e., the Young modulus E and the three-dimensional quantities K and G) can be derived as done classically. In particular, the Young modulus $E = E(\boldsymbol{e}^{tr})$ is assumed to depend on $\boldsymbol{e}^{tr}$ as follows

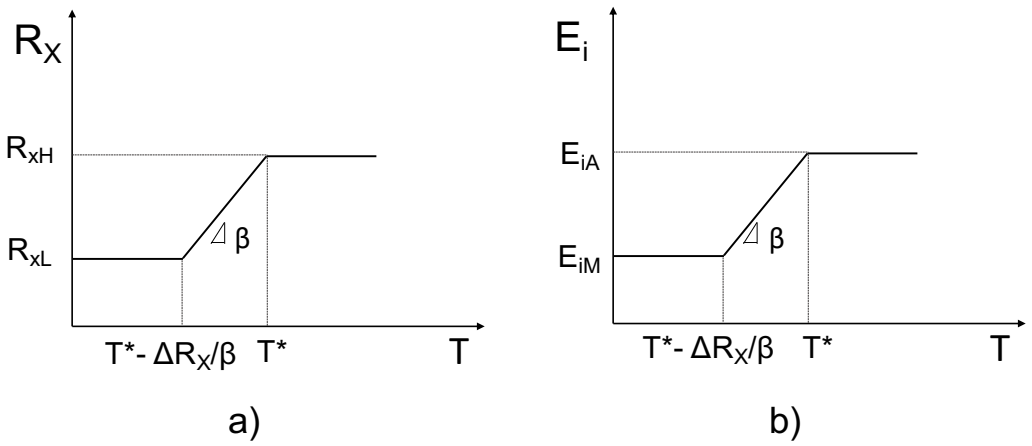


Figure 3: Temperature dependence for the elastic domain radius R_X and for the initial Young's modulus E_i.

(Auricchio et al., 2009b):

$$E = \frac{\varepsilon_L}{\dfrac{\varepsilon_L - \|\boldsymbol{e}^{tr}\|}{E_i} + \dfrac{\|\boldsymbol{e}^{tr}\|}{E_f}} \tag{17}$$

where E_i and E_f are the moduli at the beginning and the end of phase transformation. In order to take into account the Young modulus' dependence on temperature and in accordance with Eq. (16), moduli E_i and E_f are here chosen as follows:

$$E_i = \begin{cases} E_{iM} & \text{if } T \leq \left(T^* - \dfrac{\Delta R}{\beta}\right) \\ \beta \dfrac{\Delta E_i}{\Delta R}\left(T - T^*\right) + E_{iA} & \text{if } \left(T^* - \dfrac{\Delta R}{\beta}\right) \leq T \leq T^* \\ E_{iA} & \text{if } T \geq T^* \end{cases} \tag{18}$$

and

$$E_f = E_{fM} \tag{19}$$

where subscripts M and A denote martensite and austenite, respectively, and $\Delta E_i = E_{iA} - E_{iM}$ (see Figure 3.b). Moduli E_{iA}, E_{iM}, and E_f can be calibrated from stress-strain curves at different temperatures (e.g. see Figure 4).

- Parameter ε_L, measuring the maximum strain obtainable through alignment of martensite variants, can be calibrated from a uniaxial tensile curve in the fully-martensitic state (Auricchio et al., 2009b) at $T < T^* - \Delta R/\beta$ (see Figure 4).

- Parameter h^{tr}, measuring the slope of the stress-strain diagram during phase transformation, can be calibrated from a uniaxial tensile curve, e.g., in the fully-martensitic state (Auricchio et al., 2009b) at $T < T^* - \Delta R/\beta$ (see the slope of segment ending in point A' in Figure 4).

- Parameter h^p, measuring the slope of the stress-strain diagram during plastic transformation, can be calibrated from a uniaxial tensile curve, e.g., in the fully-martensitic state at $T < T^* - \Delta R/\beta$ (see the slope of segment starting from point B' in Figure 4).

- Parameter B, giving a measure of the interaction between phase transformation and plastic effects, as discussed in Section 3.2, can be calibrated from a uniaxial tensile curve, e.g., in the fully-martensitic state at $T < T^* - \Delta R/\beta$ (see point B' in Figure 4).

- Parameter $R_Y = R_Y(T)$, expressing the elastic domain radius governing plastic transformation, can be calibrated from uniaxial tensile curves at different temperatures in order to define a clear temperature-dependent law. In the following, due to the lack of appropriate experimental data, it is assumed constant with temperature and can be measured from a uniaxial tensile curve, e.g., in the fully-martensitic state at $T < T^* - \Delta R/\beta$ (see point B' in Figure 4).

To calibrate the new parameters (i.e. h^{tr}, B, and R_Y), it is possible to restrict to a one-dimensional framework. Particularly, if considering a stress-induced transformation in the fully martensitic state at $T < T^* - \Delta R/\beta$ as shown in Figure 4, the Helmholtz free-energy becomes:

$$\Psi = \frac{1}{2}\, E(\varepsilon - \varepsilon^{tr} - \varepsilon^{p} - \varepsilon^{th})^2 + \tau_M\, |\varepsilon^{tr}| + \frac{1}{2}\, h^{tr}\, (\varepsilon^{tr})^2 + \\ + \frac{1}{2}\, h^{p}\, (\varepsilon^{tr})^2 - B\varepsilon^{tr}\varepsilon^{p} + \mathcal{I}_{\varepsilon_L}(\varepsilon^{tr}) \tag{20}$$

from which the stress and thermodynamic forces are derived:

$$\begin{cases} \sigma = E(\varepsilon - \varepsilon^{tr} - \varepsilon^{p} - \varepsilon^{th}) \\ X = \sigma - \tau_M \dfrac{\varepsilon^{tr}}{|\varepsilon^{tr}|} - h^{tr}\varepsilon^{tr} + B\varepsilon^{p} - \gamma \dfrac{\varepsilon^{tr}}{|\varepsilon^{tr}|} \\ Y = \sigma - h^{p}\varepsilon^{p} + B\varepsilon^{tr} \end{cases} \tag{21}$$

Here, the Young modulus E is assumed constant. Then, substituting Eq. $(21)_1$ in $F_X = |X| - R_X(T) = 0$, the stress at the end of phase transformation (point A' in Figure 4) can be computed:

$$\sigma_{A'} = R_{XL} + h^{tr}\varepsilon_L \tag{22}$$

from which h^{tr} is calibrated. Similarly, substituting Eq. $(21)_2$ in $F_Y = |Y| - R_Y = 0$, the stress at the beginning of plastic transformation (point B' in Figure 4) can be computed:

$$\sigma_{B'} = R_Y - B\varepsilon_L \tag{23}$$

from which B and R_Y are evaluated under the convexity constraint (5). As also evident in Figure 4, the formulation is assuming that $R_Y > R_{XL} + h^{tr}\varepsilon_L > R_{XL}$.

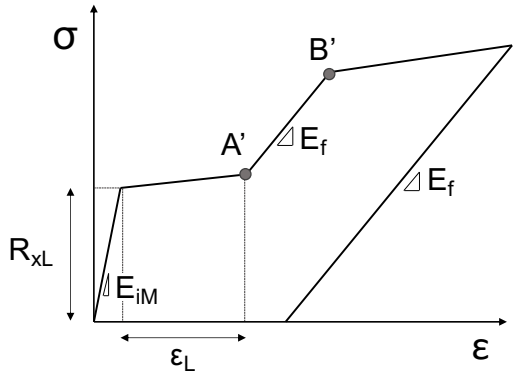


Figure 4: Graphical representation of model parameters in case of a stress-induced transformation in the fully martensitic state at $T < T^* - \Delta R/\beta$.

4. Model implementation

This section deals with the numerical implementation of model equations. For the sake of simplifying the notation, subscript $n+1$ is dropped for all the

quantities computed at the current time t_{n+1}, while subscript n is used for those computed at the previous time t_n. Then, $(\boldsymbol{e}_n^{tr}, \xi_n, \boldsymbol{e}_n^p, \mu_n, \gamma_n)$ at time t_n and $\boldsymbol{\varepsilon}$ and T at time t_{n+1} are known.

The evolution laws (24) are time-discretized by means of a backward-Euler algorithm:

$$\begin{cases} \boldsymbol{e}^{tr} = \boldsymbol{e}_n^{tr} + \Delta\xi \dfrac{\boldsymbol{X}}{||\boldsymbol{X}||} \\ \boldsymbol{e}^{p} = \boldsymbol{e}_n^{p} + \Delta\mu \dfrac{\boldsymbol{Y}}{||\boldsymbol{Y}||} \end{cases} \tag{24}$$

where $\Delta\xi = \int_{t_n}^{t_{n+1}} \dot{\xi} \ dt$ and $\Delta\mu = \int_{t_n}^{t_{n+1}} \dot{\mu} \ dt$, while all the other equations are computed at time t_{n+1}.

Therefore, the system of time-discretized equations becomes:

$$\begin{cases} \boldsymbol{e}^{tr} = \boldsymbol{e}_n^{tr} + \Delta\xi \dfrac{\boldsymbol{X}}{||\boldsymbol{X}||} \\ \boldsymbol{e}^{p} = \boldsymbol{e}_n^{p} + \Delta\mu \dfrac{\boldsymbol{Y}}{||\boldsymbol{Y}||} \\ \Delta\xi \geq 0, \ F_X \leq 0, \ \Delta\xi F_X = 0 \\ \Delta\mu \geq 0, \ F_Y \leq 0, \ \Delta\mu F_Y = 0 \\ \gamma \geq 0, \ ||\boldsymbol{e}^{tr}|| - \varepsilon_L \leq 0, \ \gamma \left(||\boldsymbol{e}^{tr}|| - \varepsilon_L \right) = 0 \end{cases} \tag{25}$$

which includes the discrete evolution laws (24), the discrete Kuhn-Tucker conditions (14), and the transformation strain constraint (1) equivalently rewritten in terms of Kuhn-Tucker conditions.

The Fischer-Burmeister complementarity function (Fischer, 1992), defined as:

$$f(a,b) = \sqrt{a^2 + b^2} + a - b \tag{26}$$

such that:

$$f(a,b) = 0 \quad \Leftrightarrow \quad b \geq 0, \ a \leq 0, \ ab = 0 \tag{27}$$

is here adopted to handle the Kuhn-Tucker conditions in system (25) (Auricchio et al., 2014; Scalet et al., 2015). Accordingly, the time-discretized Kuhn-Tucker conditions in system (25) are substituted by the time-integrated

Fischer-Burmeister complementarity functions, as follows:

$$\begin{cases} \sqrt{(F_X)^2 + (\Delta\xi)^2} + F_X - \Delta\xi = 0 \\ \sqrt{(F_Y)^2 + (\Delta\mu)^2} + F_Y - \Delta\mu = 0 \\ \sqrt{(||\boldsymbol{e}^{tr}|| - \varepsilon_L)^2 + (\gamma)^2} + (||\boldsymbol{e}^{tr}|| - \varepsilon_L) - \gamma = 0 \end{cases} \tag{28}$$

In particular, since the Fischer-Burmeister function is non-differentiable when $a = b = 0$, a regularized function (Kanzow, 1996) is adopted:

$$f_\delta(a, b) = \sqrt{a^2 + b^2 + 2\delta^2} + a - b \tag{29}$$

such that:

$$f_\delta(a, b) = 0 \quad \Leftrightarrow \quad b \geq 0,\ a \leq 0,\ ab = -\delta^2 \tag{30}$$

$\delta > 0$ being a parameter.

After substituting functions (28) in system (25), the time-discrete system of equations at time t_{n+1} is:

$$\begin{cases} \boldsymbol{e}^{tr} - \boldsymbol{e}_n^{tr} - \Delta\xi \dfrac{\boldsymbol{X}}{||\boldsymbol{X}||} = 0 \\ \boldsymbol{e}^{p} - \boldsymbol{e}_n^{p} - \Delta\mu \dfrac{\boldsymbol{Y}}{||\boldsymbol{Y}||} = 0 \\ \sqrt{(F_X)^2 + (\Delta\xi)^2} + F_X - \Delta\xi = 0 \\ \sqrt{(F_Y)^2 + (\Delta\mu)^2} + F_Y - \Delta\mu = 0 \\ \sqrt{(||\boldsymbol{e}^{tr}|| - \varepsilon_L)^2 + (\gamma)^2} + (||\boldsymbol{e}^{tr}|| - \varepsilon_L) - \gamma = 0 \end{cases} \tag{31}$$

that is solved by using the Newton-Raphson method with a line-search strategy to overcome any numerical issues associated to the use of parameter δ or to the choice of a good initial guess.

The time-discretized problem is completed by the calculus of the consistent tangent tensor which allows the quadratic convergence of the Newton-Raphson method and is expressed as:

$$\mathbb{C} = \frac{d\boldsymbol{\sigma}}{d\boldsymbol{\varepsilon}} = \frac{\partial\boldsymbol{\sigma}}{\partial\boldsymbol{\varepsilon}} + \frac{\partial\boldsymbol{\sigma}}{\partial\boldsymbol{h}} : \frac{d\boldsymbol{h}}{d\boldsymbol{\varepsilon}} = \frac{\partial\boldsymbol{\sigma}}{\partial\boldsymbol{\varepsilon}} - \frac{\partial\boldsymbol{\sigma}}{\partial\boldsymbol{h}} : \left(\frac{\partial\boldsymbol{R}}{\partial\boldsymbol{h}}\right)^{-1} \frac{\partial\boldsymbol{R}}{\partial\boldsymbol{\varepsilon}} \tag{32}$$

where $\boldsymbol{h} = \{\boldsymbol{e}^{tr}, \Delta\xi, \boldsymbol{e}^{p}, \Delta\mu, \gamma\}$ and $\boldsymbol{R}$ is system of equations (31).

Table 1: Model parameters adopted in the numerical tests.

Parameter	Value	Units
$E_{i,A}$	70000	MPa
$E_{i,M}$	30000	MPa
E_f	15000	MPa
α	$7{\cdot}10^{-6}$	$1/^{\circ}$C
ε_L	0.05	-
T^*	-18	$^{\circ}$C
β	6	MPa/$^{\circ}$C
h^{tr}	1332	MPa
h^p	900	MPa
B	1094	MPa
R_{XL}	60	MPa
R_{XH}	400	MPa
R_Y	554.7	MPa

5. Numerical results

This section presents the results of some numerical simulations and a comparison with experimental results in order to validate the model.

First, several uniaxial tests are simulated in a one-dimensional framework under strain, stress, or temperature control and compared with data obtained from the performed experimental campaign (Niccoli et al., 2018). In particular, the uniaxial experimental curve shown in Figure 2 is used to calibrate the proposed model according to the methodology detailed in Section 3.4, while free and constrained thermal recovery tests are simulated for its validation. Then, two case-studies, namely a ring-shaped coupler and a C-shaped fastener, are solved by means of a finite element analysis. For the simulation, the commercial software ABAQUS/Standard is used, after having implemented the described algorithm into a user-defined material subroutine (UMAT) by exploiting AceGen package (Korelc and Wriggers, 2016). Table 1 lists the parameters adopted in the numerical tests.

5.1. Isothermal martensitic uniaxial tests

Figure 5 shows the comparison between experimental and numerical results in terms of stress-strain curve for two values of the maximum deformation, corresponding to the lower and upper values of the pre-strain analyzed

in this investigation (respectively, $\varepsilon_{tot} = 4.8\%$ and $\varepsilon_{tot} = 28.8\%$), at constant temperature of -65°C. In particular, Figure 5.a is predicted, while Figure 5.b has been used for parameter calibration.

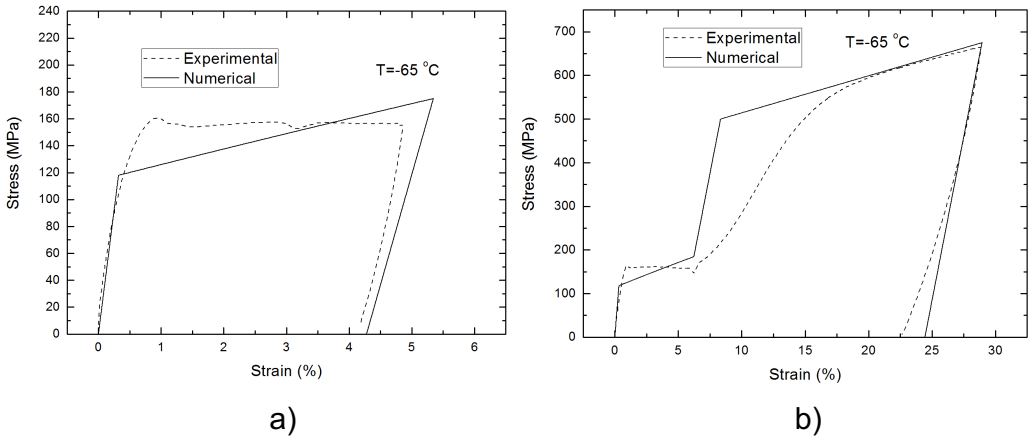


Figure 5: Comparison between stress-strain curves obtained from experiments and simulation for two values of the pre-strain: a) $\varepsilon_{tot} = 4.8\%$ (predicted) and b) $\varepsilon_{tot} = 28.8\%$ (calibrated).

It is shown that the model is able to capture all the mechanisms associated with large martensitic pre-strain, including: 1) elastic deformation of twinned martensite (M^-), 2) martensite detwinning (M^--M^+), 3) elastic deformation of detwinned martensite (M^+), and 4) plastic deformation. All these mechanisms need to be correctly simulated in such cases where SMAs experience large martensitic deformations, i.e. in case of $\varepsilon_{tot} > 10\%$.

However, both figures highlight some differences between experiments and numerical results, especially on the slopes of the detwinning and fully-detwinned curves. Such differences are, however, expected and are due to the fact that in the proposed model only tensorial internal variables are employed and, therefore, scalar and directional information are interconnected and may lead to a constrained approach. In fact, the slope of the detwinning plateau is described by the hardening parameter h^{tr}, which also governs the difference between transformation temperatures (Auricchio et al., 2009a). Therefore, a balanced value of h^{tr} has been adopted in order to describe reasonably well both detwinning plateau slope and TTs' difference. Similarly, in the model the stiffness modulus of fully-detwinned martensite is always defined by E_f (in the presence or not of plastic strains), while in the

experimental evidences more complex effects take place (Figure 5.b). The difference between twinned martensite moduli in Figure 5.a is due physical phenomena, observable experimentally, associated to changes in the martensite variant structures occurring at the beginning of the reorientation process, that result in non-linear contributions even at very small stress amplitude (Liu et al., 1998). Finally, it is worth noting that precise stress-strain ranges for the four different mechanisms shown in Figure 5.b cannot be defined in polycrystalline alloys, since they could coexist at the microstructural scale depending on the grain orientation, as confirmed by the unsharpened shape of the stress-strain curves in the transition regions. On the contrary, sharp changes are given by the model, as shown in Figure 5.b, according to well-defined material parameters.

5.2. Free thermal recovery

The effects of mechanical pre-strain on both shape memory properties and on TTs were systematically analyzed. Figures 6 reports the values of ε_{OW}, ε_{TW}, ε_{res}, and ε_P as a function of the total strain ε_{tot}. In particular, Figures 6.a and 6.b show the experimental and numerical results, respectively. As expected, the shape memory properties of the alloy, in terms of both ε_{OW} and ε_{TW}, are significantly affected by the pre-strain ε_{tot}. In particular, a marked increase of ε_{OW} is observed up to a maximum value of about 8.4% at $\varepsilon_{tot} = 14.4\%$, followed by a decrease with further increasing the pre-strain. This is a direct consequence of the slips occurring in the martensitic matrix at such large mechanical pre-strain, as confirmed by the marked increase of the permanent strain ε_P. A similar trend is observed for ε_{TW}, with a maximum value of about 4.0% obtained at higher values of the pre-strain ($\varepsilon_{tot} = 24\%$). In fact, it is well known that plastic deformation would benefit the two-way shape memory properties of SMAs, as dislocation structures generate favorably oriented martensitic variants, mainly responsible of the TW-SME. The decreasing trend due to slips for increasing pre-strains is however not described by the model, since it is macro-phenomenological and does not concern the complicated microstructure of the alloy and its evolution during thermo-mechanical deformation. Moreover, it is recalled that the increase in retained martensite due to accumulated plastic deformation (Heller et al., 2019; Shaw and Kyriakides, 1995; Yan et al., 2003) is not taken into account by the proposed model.

As discussed in Section 1, large pre-strain values (15-25%) cause marked increase of the austenite TTs at the first cycle. Figure 7 illustrates the

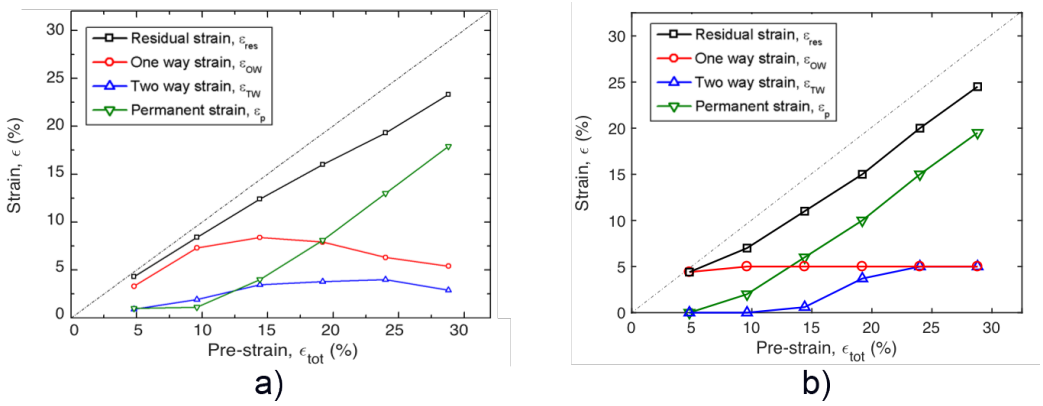


Figure 6: Evolution of shape memory strains (ε_{OW} and ε_{TW}), residual and permanent strains (ε_{res} and ε_P) as a function of the total pre-strain (ε_{tot}): a) experimental data and b) predicted numerical results.

evolution of austenite TTs (A_s^{1st} and A_f^{1st}) together with the increase of the austenite peak temperature with respect to the base material ($\Delta A_p^{1st} = A_p^{1st} - A_p$). In particular, experimental data are shown in Figure 7.a and predicted numerical results are shown in Figure 7.b. A marked increase (about 50°C) is observed for ε_{tot} around 10%, and a subsequent slight increase with further increasing $\varepsilon_{tot} = 24\%$, with differences of about 60°C at the maximum pre-strain ($\varepsilon_{tot} = 28.8\%$). The comparison between Figures 7.a and 7.b shows that the model is able to correctly simulate this mechanism, which is a critical aspect when dealing with severe martensitic deformations.

5.3. Constrained thermal recovery

The constrained recovery capabilities of the alloy were analyzed by thermal cycles after mechanical pre-strain by holding the residual strain ε_{res}. This was obtained by performing strain-controlled thermal tests on pre-deformed samples and by measuring the recovery stress, σ_{rec} (see Figure 8.a). The thermal cycle consisted in a heating up to 200°C and subsequent cooling down to -65°C. The test was carried out with the aim of measuring the maximum recoverable force of the alloy, as well as to analyze the shift in the TTs under applied stress conditions, in the case of pre-strain equal to 18 %, as shown in Figure 8. Such a pre-deformation level was chosen as it corresponds to a significant austenitic TTs shift as well as to a remarkable TW behavior (see Figure 7). In this testing condition, the whole residual strain was prevented, in order to obtain the maximum recovery force and, consequently,

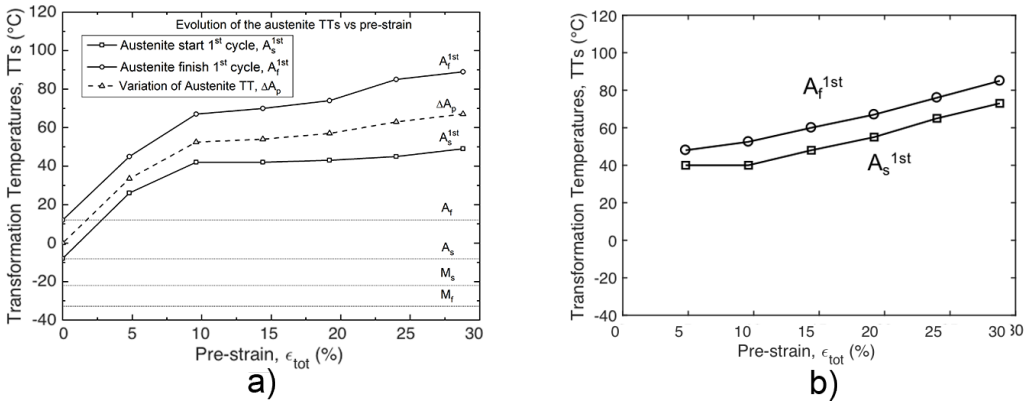


Figure 7: Evolution of transformation temperatures (TTs) as a function of the total pre-strain (ε_{tot}): a) experimental measurements and b) predicted numerical results.

the maximum increase of the martensite TTs. It is worth pointing out that A_f^σ in Figure 8.a corresponds to the temperature at which the SMA sample, under stress, becomes fully austenitic, i.e. without thermally-induced or stress-induced martensitic variants. A_f^σ corresponds indicatively to MD (Martensite desist temperature) for the first heating cycle. A drop of the recovery stress, is recovered by cooling below M_s^σ due to the two-way recovery capability of the alloy. Furthermore, Figure 8.a shows that a compression state occurs in the material when the temperature approach M_f, as the two way strain is prevented.

The comparison between experiments (Figure 8.a) and predicted simulations (Figure 8.b) demonstrates that the model is able to simulate the development of recovery forces. The stress evolution with temperature is captured correctly in both heating and cooling phases. The stress-temperature slope mismatch between experiments and simulations occurring during the early stage of cooling (from about 200 °C to 50 °C) is mainly attributed to the austenite Young's modulus variation with temperature (Duerig et al., 1990; Šittner et al., 2001, 2000), which is not modelled. Furthermore, Figure 8.b shows the evolution of plastic strains as a function of temperature during the recovery test. It is worth noting that they accumulate not only during the severe isothermal pre-strain phase, but also during the constrained thermal recovery, where SIM variants transform to austenite involving slip deformations (Šittner et al., 2018).

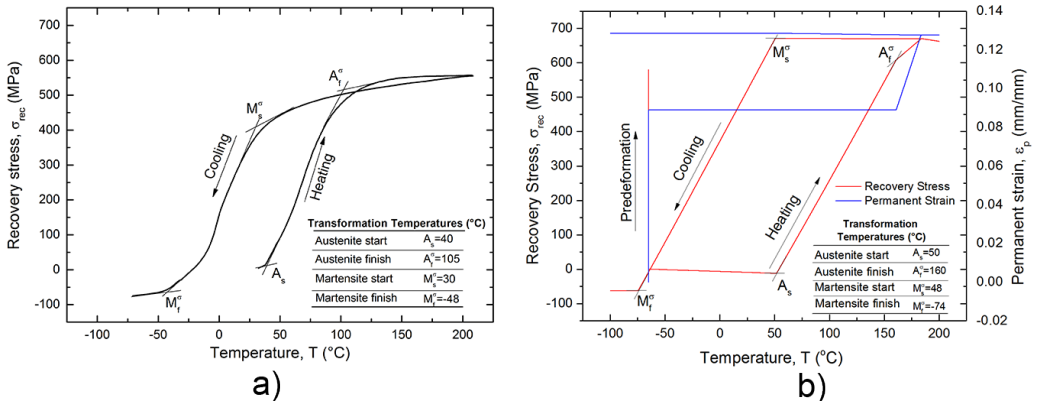


Figure 8: Recovery force and stress (F_{rec} and σ_{rec}) under constrained thermal cycles ($\varepsilon = \varepsilon_{res}$) for a mechanical pre-strain ((ε_{tot})) equal to 18 %: a) experimental measurements and b) predicted numerical results.

5.4. Case studies

The model is verified by two different case studies, involving both three-dimensional geometries and non-uniform stress-strain distributions. The case study #1 is a ring-shaped SMA coupler, to be used for pipe coupling, similar to the one analyzed in Niccoli et al. (2017a,b). The case study #2 is a C-shaped fastener for possible use as a flange coupler. Both the pre-strain application and the subsequent thermal recovery are simulated. In particular, the shift of the austenite TTs at the first thermal activation and the shape memory properties have been analyzed, in terms of both OW-SME and TW-SME.

5.4.1. Case studies #1

Figure 9.a shows the geometry and dimensions of the SMA ring, while 9.b illustrates the finite element model used for the numerical simulation. One-eight of geometry is modeled, due to axial symmetry, by using 26400 full integration 8-node hexahedral elements (C3D8) and 29716 nodes. A mesh refinement has been performed to adopt the appropriate mesh size.

Martensitic pre-strain is simulated by applying a pressure on the inner surface of the ring, corresponding to a circumferential strain ($\varepsilon_{\theta i} = u_i/r_i$, where u_i is the displacement at the inner ring diameter $2 \cdot r_i$) equal to 18%. This value is selected based on the results obtained from uniaxial tests (see Section 5.1).

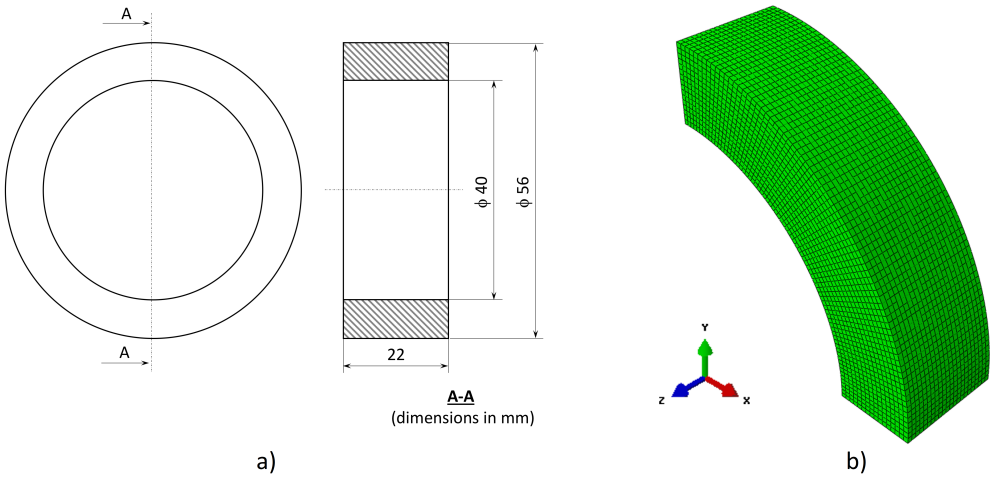


Figure 9: SMA ring for pipe coupling: a) geometry and dimension and b) finite element discretization.

Figures 10.a and 10.b illustrate, respectively, the plastic strain distribution $\|\boldsymbol{e}^p\|$ and the von Mises stress distribution σ_{VM} in the SMA ring after martensitic pre-strain and subsequent complete unloading. Results reveal significant residual stresses at the internal diameter, close to 160 MPa, as a consequence of a marked plastic deformations of about 13%. Compression stresses occur at the internal diameter, while tensile stresses at the outer radius of the ring. In addition, the maximum allowable transformation strain ($\|\boldsymbol{e}^{tr}\|$= 5%) is reached in the whole cross section of the ring.

Figure 11 illustrates the stress-free strain-temperature response of a trained ring obtained from a complete thermal cycle between the TTs. In particular, the circumferential strain at the inner diameter ($\varepsilon_{\theta i} = u_i/r_i$, right vertical axis) and the internal diameter variation (ΔD_i, left vertical axis) are shown in the graph. A OW strain $\varepsilon_{OW} = 5.0\%$ is recorded. It corresponds to an internal diameter contraction $\Delta D_{iOW} = 2.1$ mm. A remarkable TW behavior is also obtained with $\varepsilon_{TW} = 1.4\%$ and $\Delta D_{iTW} = 0.51$ mm. The figure also shows the TTs of the SMA ring at the first thermal cycle (M_s, M_f, A_s and A_f). The results are similar to those obtained in the uniaxial tests (see Figure 5), although triaxial strain fields are generated for this geometry.

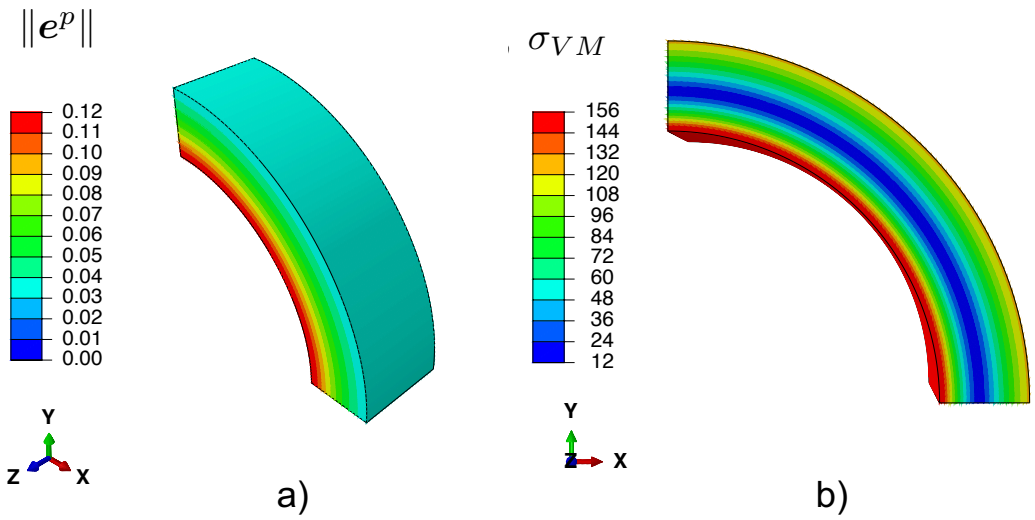


Figure 10: Finite element results of the SMA ring after martensitic pre-strain and unloading. Contour plot of the (a) plastic strain tensor norm, $\|e^p\|$, and (b) von Mises stress, σ_{VM} (MPa).

5.4.2. Case studies #2

Figure 12.a shows the geometry and dimensions of the SMA C-shaped fastener, while Figure 12.b illustrates the finite element model used for numerical simulation. One-half of geometry is modeled, due to axial symmetry, by using 28080 full integration 8-node hexahedral elements (C3D8) and 31773 nodes. Again, a mesh refinement has been performed.

Martensitic pre-strain is simulated by applying a pressure of 150 MPa at extremity of the C, on the rectangular surface whose trace corresponds to the AB segment in Figure 12.a.

Plastic strain, $\|e^p\|$, and transformation strain, $\|e^{tr}\|$, distributions in the SMA element after martensitic pre-strain and unloading are reported in Figure 13.a and b, respectively. Results reveal a significant yielding of the fastener. In fact, the pre-strain induces a large bending moment in the fastener with maximum permanent strain of about 27% (see Figure 13.a). In addition, Figure 13.b shows that the maximum allowable transformation strain ($\|e^{tr}\| = 5\%$) is reached in most of the fastener volume.

Figure 14 illustrates the stress-free strain-temperature response of a trained C-shaped element obtained from a thermal cycle between the TTs. The OW and TW capabilities of the element are analyzed in terms of horizontal dis-

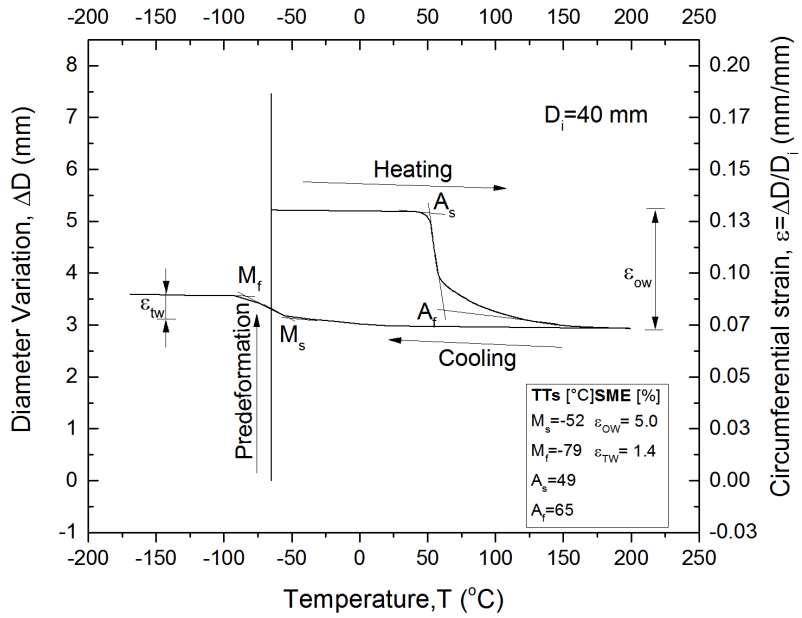


Figure 11: Finite element results of the SMA ring thermal recovery. Internal diameter variation-temperature ($\Delta D_i - T$) and strain-temperature ($\varepsilon_{\theta i} - T$) curve obtained for martensitic pre-strain ($\varepsilon_{\theta i0} = u_{i0}/r_i$ =18%) and the first stress-free thermal activation between the TTs.

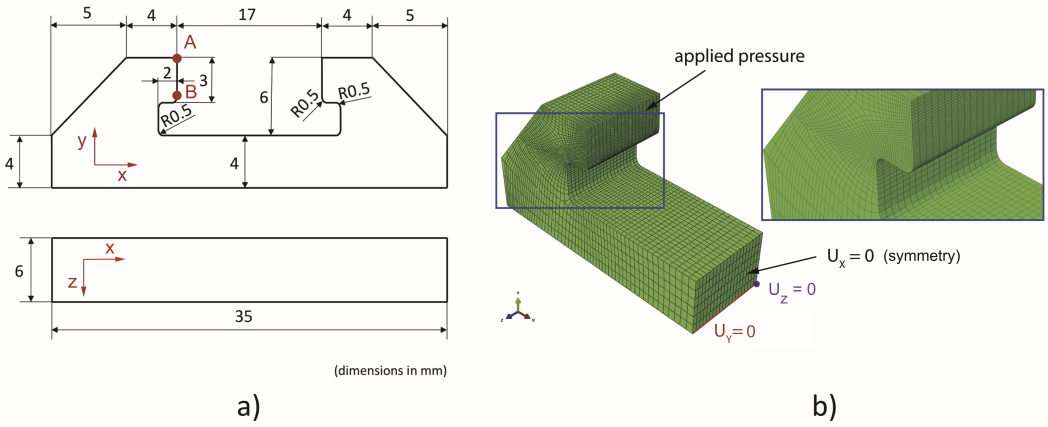


Figure 12: C-shaped SMA fastener: a) geometry and dimension and b) finite element discretization.

placement of the fastener extremity (point A in Figure 12.a). An horizontal

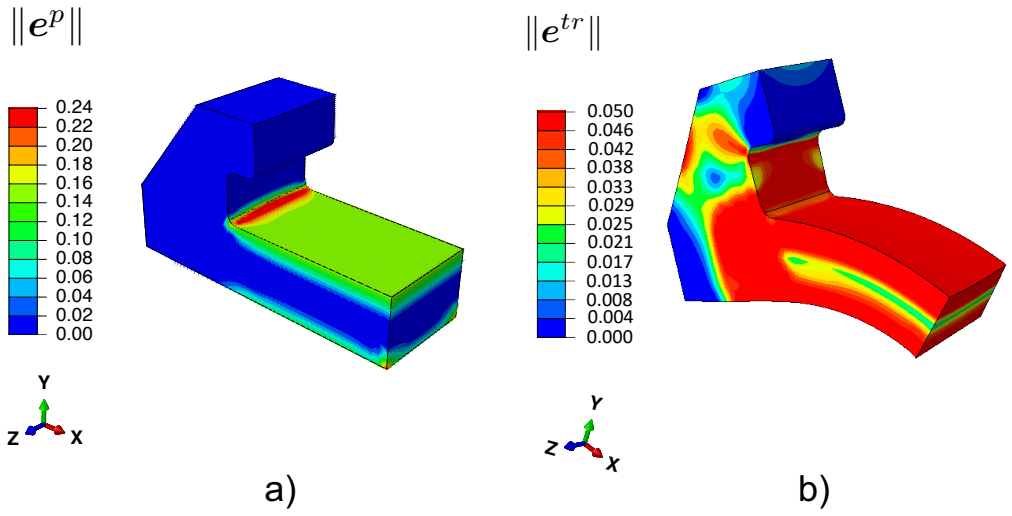


Figure 13: Finite element results of the SMA fastener after martensitic pre-strain and unloading. Contour plot of the (a) plastic strain tensor norm, $\|e^p\|$, and (b) transformation strain tensor norm, $\|e^{tr}\|$.

displacement of about 10 mm is induced during the pre-deformation stage. A OW displacement $u_{TW} = 3.62$ mm and a TW displacement $u_{TW} = 0.41$ mm are obtained. The figure also shows the TTs of the SMA fastener at the first thermal cycle (M_s, M_f, A_s, and A_f). The functional behavior of the element is comparable to the uniaxial and biaxial geometries analyzed previously.

6. Conclusions

The present paper has proposed a generalization of the three-dimensional phenomenological constitutive model by Souza et al. (1998) in order to describe the behavior of severely pres-strained NiTi-based SMAs. The proposed model has been validated on experimental data and two applicative examples have been studied. Advantages in using the proposed model derive from its direct numerical implementation, based on the Fischer-Burmeister complementarity function, and from a limited number of parameters that can be calibrated from uniaxial experiments. The great versatility of the model will allow to include typical effects of material behavior under cyclic loading, which are not accounted in the present work, such as permanent inelasticity (Auricchio et al., 2007; Heller et al., 2019; Peigney et al., 2018)

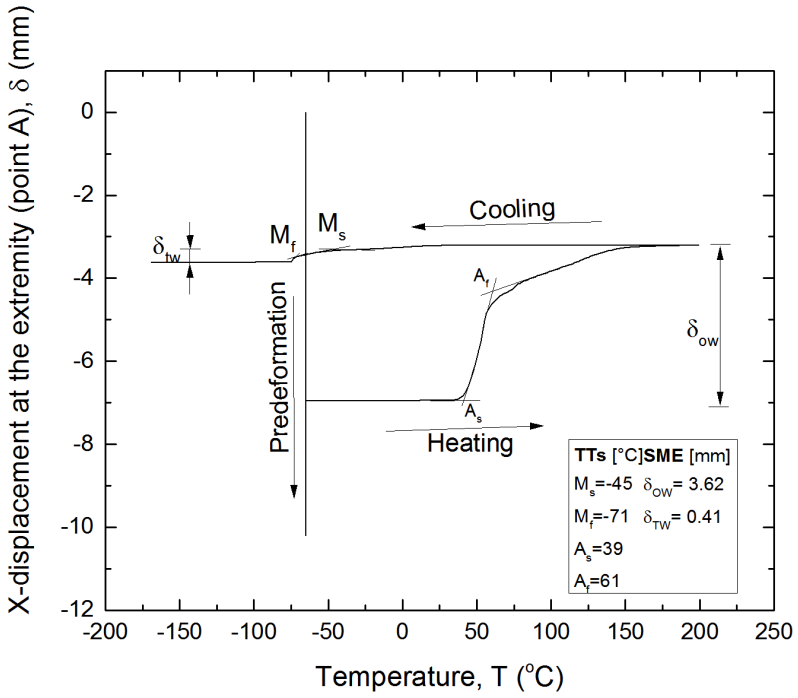


Figure 14: Finite element results of a thermal recovery for the C-shaped fastener. Horizontal displacement-temperature ($\delta - T$) curve for the element extremity (point A in Figure 12) obtained for the martensitic pre-strain ($\delta_{max} = 10$ mm) and the first stress-free thermal activation between the TTs.

and partial transformation response (Karakalas et al., 2019). Moreover, the achieved results demonstrate the possibility of using the model for the design of components under such a complex SMA material behavior. To this purpose, ongoing work will focus on an extensive experimental campaign to validate the model on multiaxial loading cases and on model extension to finite strains.

References

Ashrafi, M., 2019. Constitutive modeling of shape memory alloys under cyclic loading considering permanent strain effects. Mechanics of Materials 129, 148–158.

Auricchio, F., Bonetti, E., Scalet, G., Ubertini, F., 2014. Theoretical and numerical modeling of shape memory alloys accounting for multiple phase

transformations and martensite reorientation. International Journal of Plasticity 59, 30–54.

Auricchio, F., Coda, A., Reali, A., Urbano, M., 2009a. SMA numerical modeling versus experimental results: Parameter identification and model prediction capabilities. Journal of Materials Engineering and Performance 18, 649–654.

Auricchio, F., Marfia, S., Sacco, E., 2003. Modeling of SMA materials: training and two way memory effects. Computers & Structures 81 (24), 2301–2317.

Auricchio, F., Petrini, L., 2004. A three-dimensional model describing stress-temperature induced solid phase transformations: solution algorithm and boundary value problems. International Journal for Numerical Methods in Engineering 61, 807–836.

Auricchio, F., Reali, A., Stefanelli, U., 2007. A three-dimensional model describing stress-induced solid phase transformation with residual plasticity. International Journal of Plasticity 23, 207–226.

Auricchio, F., Reali, A., Stefanelli, U., 2009b. A macroscopic 1D model for shape memory alloys including asymmetric behaviors and transformation-dependent elastic properties. Computer Methods in Applied Mechanics and Engineering 198, 1631–1637.

Barrera, N., Biscari, P., Urbano, M., 2014. Macroscopic modeling of functional fatigue in shape memory alloys. European Journal of Mechanics - A/Solids 45, 101–109.

Bo, Z., Lagoudas, D., 1999. Thermomechanical modeling of polycrystalline SMAs under cyclic loading, part III: evolution of plastic strains and two-way shape memory effect. International Journal of Engineering Science 37 (9), 1175–1203.

Duerig, T., Melton, K., Stockel, D., Wayman, C., 1990. Engineering Aspects of Shape Memory Alloys. Butterworth-Heinemann Ltd, London.

Evangelista, V., Mara, S., Sacco, E., 2009. Phenomenological 3D and 1D consistent models for shape-memory alloy materials. Computational Mechanics 44, 405–421.

Fischer, A., 1992. A special Newton-type optimization method. Optimization 24, 269–284.

Govindjee, S., Kasper, E., 1997. A shape memory alloy model for uranium-niobium accounting for plasticity. Journal of Intelligent Material Systems and Structures 8, 815–823.

Grandi, D., Stefanelli, U., 2015. The Souza-Auricchio model for shape-memory alloys. Discrete and Continuous Dynamical Systems Series S 8 (4), 723–747.

Hartl, D., Lagoudas, D., 2009. Constitutive modeling and structural analysis considering simultaneous phase transformation and plastic yield in shape memory alloys. Smart Materials and Structures 18, 104017.

Hebda, D., White, S., 1995. Effect of training conditions and extended thermal cycling on Nitinol two-way shape memory behavior. Smart Materials and Structures 4 (4), 298–304.

Heller, L., Sittner, P., Sedlák, P., Seiner, H., Ty, O., Kaderaveka, L., Sedmak, P., Vronka, M., 2019. Beyond the strain recoverability of martensitic transformation in niti. International Journal of Plasticity 116, 232–264.

Humbeeck, J., 2001. Shape memory alloys: A material and a technology. Advanced Engineering Materials 3 (11), 837–850.

Jani, J., Leary, M., Subic, A., Gibson, M., 2014. A review of shape memory alloy research, applications and opportunities. Materials and Design 56, 1078–1113.

Jiang, D., Landis, C., 2016. A constitutive model for isothermal pseudoelasticity coupled with plasticity. Shape Memory and Superelasticity 2, 360–370.

Kanzow, C., 1996. Some noninterior continuation methods for linear complementarity problems. SIAM Journal on Matrix Analysis and Applications 17, 851–868.

Karakalas, A., Machairas, T., Solomou, A., Saravanos, D., 2019. Modeling of partial transformation cycles of SMAs with a modified hardening function. Smart Materials and Structures 28, 035014.

Khalil, W., Mikolajczak, A., Bouby, C., Ben Zineb, T., 2012. A constitutive model for Fe-based shape memory alloy considering martensitic transformation and plastic sliding coupling: application to a finite element structural analysis. Journal of Intelligent Material Systems and Structures 23 (10), 1143–1160.

Kirkby, E., Rule, J., Michaud, V., Sottos, N., White, S., Manson, J.-A., 2008. Embedded shape-memory alloy wires for improved performance of self-healing polymers. Advanced Functional Materials 18 (15), 2253–2260.

Korelc, J., Wriggers, P., 2016. Automation of Finite Element Methods. Springer International Publishing.

Lagoudas, D., Entchev, P., 2004. Modeling of transformation-induced plasticity and its effect on the behavior of porous shape memory alloys. Part I: constitutive model for fully dense SMAs. Mechanics of Materials 36, 865–892.

Lexcellent, C., Leclercq, S., Gabry, B., Bourbon, G., 2000. The two way shape memory effect of shape memory alloys: an experimental study and a phenomenological model. International Journal of Plasticity 16 (10-11), 1155–1168.

Lin, H., Wu, S., 1993. Determination of heat of transformation in a cold-rolled martensitic TiNi alloy. Metallurgical and Materials Transactions A 24A, 293–299.

Liu, Y., Liu, Y., Van Humbeeck, J., 1998. Two-way shape memory effect developed by martensite deformation in NiTi. Acta Materialia 47 (1), 199–209.

Liu, Y., McCormick, P., 1990. Factors influencing the development of two-way shape memory in NiTi. Acta Metallurgica et Materialia 38 (7), 1321–1326.

Malukhin, K., Sung, H., Ehmann, K., 2012. A shape memory alloy based tool clamping device. Journal of Materials Processing Technology 212, 735–744.

Niccoli, F., Garion, C., Maletta, C., Chiggiato, P., 2017a. Shape memory alloy-based pipe couplers for ultra-high vacuum applications in particle

accelerators: design and experimental assessment. Journal of Vacuum Science and Technology A 35 (3), 031601.

Niccoli, F., Garion, C., Maletta, C., Chiggiato, P., 2018. Shape memory alloy technologies for ultra-high vacuum coupling in particle accelerators. In: Proceedings of ESOMAT 2018 – 11th European Symposium on Martensitic Transformations. Metz, France.

Niccoli, F., Garion, C., Maletta, C., Sgambitterra, E., Furgiuele, F., Chiggiato, P., 2017b. Beam-pipe coupling in particle accelerators by shape memory alloy rings. Materials and Design 114, 603–611.

Otsuka, K., Ren, X., 2005. Physical metallurgy of Ni-Ti-based shape memory alloys. Progress in Materials Science 50, 511–678.

Otuska, K., Wayman, C., 1998. Shape Memory Materials. Cambridge University Press, Cambridge.

Paiva, A., Savi, M., Braga, A., Pacheco, P., 2005. A constitutive model for shape memory alloys considering tensile-compressive asymmetry and plasticity. International Journal of Solids and Structures 42, 3439–3457.

Peigney, M., Scalet, G., Auricchio, F., 2018. A time integration algorithm for a 3D constitutive model for SMAs including permanent inelasticity and degradation effects. International Journal for Numerical Methods in Engineering 115 (9), 1053–1082.

Petrini, L., Bertini, A., Berti, F., Pennati, G., Migliavacca, F., 2017. The role of inelastic deformations in the mechanical response of endovascular shape memory alloy devices. Proceedings of the Institution of Mechanical Engineers, Part H: Journal of Engineering in Medicine 231 (5), 391–404.

Piao, M., Otsuka, K., Miyazaki, S., Horikawa, H., 1993. Mechanisms of As temperature increase by pre-deformation in thermoelastic alloys. Materials Transactions 34 (1), 919–929.

Rogueda, C., Vacher, P., Lexcellent, C., Contardo, L., Guenin, G., 1991. Pseudoelastic behavior and two way memory effect in Cu-Zn-Al alloys. Journal de Physique IV 1 (C4), 409–414.

Saint-Sulpice, L., Arbab Chirani, S., Calloch, S., 2007. A 3D super-elastic model for shape memory alloys taking into account progressive strain under cyclic loadings. Mechanics of Materials 41 (1), 12–26.

Scalet, G., Auricchio, F., Bonetti, E., Castellani, L., Ferri, D., Pachera, M., Scavello, F., 2015. An experimental, theoretical and numerical investigation of shape memory polymers. International Journal of Plasticity 67, 127–147.

Sehitoglu, H., Karaman, I., Anderson, R., Zhang, X., Gall, K., Maier, H., Chumlyakov, Y., 2000. Compressive response of NiTi single crystals. Acta Materialia 48, 3311–3326.

Shaw, J., Kyriakides, S., 1995. Thermomechanical aspects of NiTi. Journal of the Mechanics and Physics of Solids 43, 1243–1281.

Siegert, W., Neuking, K., Mertmann, M., Eggeler, G., 2003. First cycle shape memory effect in the ternary NiTiNb system. Journal de Physique IV 112, 739–742.

Souza, A., Mamiya, E., Zouain, N., 1998. Three-dimensional model for solids undergoing stress-induced phase transformations. European Journal of Mechanics A/Solids 17, 789–806.

Tabesh, M., Boyd, J., Atli, K., Karaman, I., Lagoudas, D., 2018. Design, fabrication, and testing of a multiple-actuation shape memory alloy pipe coupler. Journal of Intelligent Material Systems and Structures 29 (6), 1165–1182.

Tan, G., Liu, Y., 2004. Comparative study of deformation-induced martensite stabilization via martensite reorientation and stress-induced martensitic transformation in NiTi. Intermetallics 12, 373–381.

Šittner, P., Lukáš, P., Novák, V., Neov, D., Cerettin, M., 2001. In situ neutron diffraction study of stresses generated by shape memory alloys. Journal of Neutron Research 9, 143–150.

Šittner, P., Sedlák, P., Seiner, H., Sedmák, P., Pilcha, J., Delville, R., Heller, L., Kadeřávek, L., 2018. On the coupling between martensitic transformation and plasticity in NiTi: Experiments and continuum based modelling. Progress in Material Science 98, 249–298.

Šittner, P., Vokoun, D., Dayananda, G., Stalmans, R., 2000. Recovery stress generation in shape memory Ti50Ni45Cu5 thin wires. Materials Science and Engineering A 286, 298–231.

Wang, M., Jiang, M., Liao, G., Guo, S., Zhao, X., 2012. Martensitic transformation involved mechanical behaviors and wide hysteresis of NiTiNb shape memory alloys. Progress in Natural Science: Materials International 22 (2), 130–138.

Wang, X., Xu, B., Yue, Z., 2007. Micromechanical modelling of the effect of plastic deformation on the mechanical behavior in pseudoelastic shape memory alloys. International Journal of Plasticity 24, 1307–1032.

Xu, L., Solomou, A., Lagoudas, D., 2019. A three-dimensional constitutive modeling for shape memory alloys considering two-way shape memory effect and transformation-induced plasticity. In: AIAA Scitech 2019 Forum. pp. 1–12.

Xu, Y., Otsuka, K., Toyama, N., Yoshida, H., Nagai, H., Kishi, T., 2003. Additive nature of recovery strains in heavily cold-worked shape memory alloys. Scripta Materialia 48, 803–8.

Yan, W., Wang, C., Zhang, X., Mai, Y., 2003. Theoretical modeling of the effect of plasticity on reverse transformation in superelastic shape memory alloys. Materials Science and Engineering A 354, 146–157.

Yan, X., Ge, Y., Van Humbeeck, J., 2016. Influence of different thermomechanical cycling routes on recovery stresses of annealed NiTi wires. Journal of Materials Engineering and Performance 25 (1), 267–273.

Yan, X., Van Humbeeck, J., 2013. Temperature and time dependence on recovery stress relaxation in Nickel Titanium wire during isothermal holding at high temperatures. Strain 49 (5), 451–455.

Zaki, W., Moumni, Z., 2007. A 3D model of the cyclic thermomechanical behavior of shape memory alloys. Journal of the Mechanics and Physics of Solids 55 (11), 2427–2454.

Zhang, Y., Cheng, Y., Grummon, D., 2007. Finite element modeling of indentation-induced superelastic effect using a three-dimensional constitutive model for shape memory materials with plasticity. Journal of Applied Physics 101, 1–6.